Journal of Membrane Science 638 (2021) 119681

Contents lists available at ScienceDirect

Journal of Membrane Science

journal homepage: www.elsevier.com/locate/memsci

Shape of nanopores in track-etched polycarbonate membranes

Shankar Dutt [a,*], Pavel Apel [b], Nikolay Lizunov [b], Christian Notthoff [a], Qi Wen [a], Christina Trautmann [c,d], Pablo Mota-Santiago [e], Nigel Kirby [e], Patrick Kluth [a]

[a] Department of Electronic Materials Engineering, Research School of Physics, Australian National University, Canberra ACT 2601, Australia
[b] Flerov Laboratory of Nuclear Reactions, Joint Institute for Nuclear Research, 141980, Dubna, Moscow region, Russia
[c] GSI Helmholtzzentrum für Schwerionenforschung, Planckstr. 1, 64291, Darmstadt, Germany
[d] Technische Universtät Darmstadt, 64289, Darmtadt, Germany
[e] ANSTO-Australian Synchrotron, Melbourne, Australia

ARTICLE INFO

Keywords:
Track-etched membranes
Nanopore shape
Polycarbonate
Small angle X-ray scattering
Ion track halo

ABSTRACT

High aspect-ratio nanopores of nearly cylindrical geometry were fabricated by irradiation of 20 μm thick polycarbonate (PC) foils with Pb ions followed by UV sensitization and etching in 5 M NaOH at 60 °C. Synchrotron-based small-angle X-ray scattering (SAXS) was used to study the morphology and size variation of the nanopores as a function of the etching time and ion fluence. The shape of the nanopores was found to be consistent with cylindrical pores with ends tapering off towards the two polymer surfaces in the last ~1.6 μm. The tapered structure of the nanopores in track-etched PC membranes was first observed more than 40 years ago followed by many other studies suggesting that the shape of nanopores in PC membranes deviates from a perfect cylinder and nanopores narrow towards both membrane surfaces. It was also reported that the transport properties of the nanopore membranes are influenced by the tapered structure. However, quantification of the shape of nanopores has remained elusive due to inherent difficulties in imaging the pores using microscopy techniques. The present manuscript reports on the quantitative measurement of the tapered structure of nanopores using SAXS. Determination of this structure was enabled by obtaining high quality SAXS data and the development of appropriate fitting models. The etch rates for both the radius at the polymer surface and the radius of the pore in bulk were calculated. Both etch rates decrease slightly with increasing fluence. This behavior is ascribed to the overlap of track halos which are characterized by cross-linking of the polymer chains. The halo radius was estimated to be approximately 120 nm. The influence of the observed nanopore shape on the pore transport properties was estimated and found to have a significant influence on the water flow rates compared to cylindrical pores. The results enable a better understanding of track-etched membranes and facilitate improved pore design for many applications.

1. Introduction

When a material is irradiated with heavy ions in the MeV-GeV range, the ions can create a narrow damage trail along their path governed by the interaction with the materials' electrons. In particular, in polymers, these so-called 'ion tracks' are significantly more susceptible to chemical etching than the undamaged material and can thus be used to fabricate nanopores. By selecting suitable irradiation and etching conditions, the size and to some extent the shape of the pores can be controlled. The first track-etched membrane was fabricated from a polycarbonate film in 1963 [1], and production of such membranes, using fission fragments as bombarding particles, under the trademark "Nuclepore®" began soon after [2]. Since the 1970s, track-etched membranes have become an indispensable tool for several applications, including laboratory filtration, water filtration, cell culture growth, and environmental studies [2,3]. In the 1980s, advances in heavy-ion accelerator technology resulted in the replacement of the fission-fragments with high-energy charged ions [4,5]. Nowadays, several facilities provide ion beams for the commercial production of ion-track membranes. The tracks and consequently the pores are aligned parallel and are randomly distributed over the irradiation surface. The track density is easily adjusted between a single ion per sample and up to 10^{10} ions cm^{-2} or more by adjusting the ion fluence. Under suitable etching conditions, the tracks are converted into uniform nanopores with an extremely narrow size distribution.

* Corresponding author.
E-mail address: shankar.dutt@anu.edu.au (S. Dutt).

https://doi.org/10.1016/j.memsci.2021.119681
Received 18 April 2021; Received in revised form 14 June 2021; Accepted 31 July 2021
Available online 4 August 2021

These properties make the membranes interesting for specific filtration applications and for the transport of liquids, gases, particles, solutes, and electrolytes. Also, research on electromagnetic waves in restricted volumes and selective interaction processes of molecules and ions with the chemically or physically modified nanopore surface has attracted great interest due to emerging applications in life science and nanotechnology (see examples of historical and recent reviews [2–12] and some landmark original papers [13–22]).

The ion track technology is usually applied to few polymers, including polyethylene terephthalate (PET), polycarbonate (PC), and polyimide [5]. One of the most versatile and intensively studied materials for nanopore fabrication is polycarbonate because of its excellent mechanical and chemical properties and because the pores are well defined and have a very small size distribution [23–25].

It is generally assumed that nanopores created through the track-etch technology in PC membranes are cylindrical; however, this is only a crude approximation of the actual pore structure. In the past [14, 26–31], it has been reported that the structure of the pores is tapered towards the surface. D. Cannell and F. Rondelez [14] were the first to report this feature for PC nanopore membranes. They measured the diffusion of polystyrenes dissolved in ethyl acetate through nanopore membranes. To characterize the nanopores, the authors measured the flow of water and ethyl acetate through the nanopores and calculated the pore size using Poiseuille's equation. They concluded that the pores have 'small lips' at the surface with an opening smaller in diameter than the inner pore. A. Hernandez et al. [26] investigated the porosity of several Nuclepore® polycarbonate membranes employing a pycnometric method (utilizing the mass difference between a membrane inside the pycnometer with pure water and a dry membrane). They found that the porosity calculated from microscopy images was different and implied that the pores are not cylindrical but have a 'barrel-like' geometry. The shape of the nanopores can also be inferred by using the membranes as templates for growing nanowires. This technique delivered similar results. C. Schönenberger et al. [27] observed that the nanowires grown are not cylindrical but are tapered towards the ends and suggested that the pores have a 'cigar-like' structure. E. Ferain and R. Legras [28] obtained similar results using nanopores in PC to grow cobalt nanowires describing the shape as 'toothpick' like observing that the grown nanowires are tapered towards the ends. J. Duchet et al. [29] synthesized polypyrrole (PPy) in the pores of PC. They also found that the PPy tubules have a "cigar-like" shape resulting from the non-cylindrical shape of the nanopores in the PC membrane. Cornelius et al. [32] compared SAXS data with SEM data and found systematic smaller pore radii for SEM measurements. However, no quantitative measurements of this structure of the pores and how it evolves with etching time and ion fluence have been reported to date.

In this paper, we report the characterization of the nanopore shape and size in PC membranes as a function of the irradiation fluence with high precision using synchrotron-based small-angle X-ray scattering (SAXS) complemented by scanning electron microscopy (SEM). SAXS is based on the elastic scattering of monochromatic X-rays that result from density fluctuations on the nanometer to micrometer scale [33–36]. Ion tracks or track-etched nanopores embedded in the polymer matrix act as scattering objects of reduced density. SAXS allows the accurate determination of their size and shape in a non-destructive manner in particular for parallel and monodisperse structures [37–40]. SAXS can provide accurate and statistically reliable information because the measured scattering intensity results from hundreds of thousands of pores. To derive the nanopore morphology from the scattering curves, detailed modelling of various contributions to the scattering intensity needs to be done, and a suitable real space model assumption is used to develop the fitting model. The quality of the scattering data also determines the complexity of the model that can be resolved. Several previous studies that utilize SAXS to study nanopores in PC considered the pores to be cylindrical and have employed a cylinder model for the analysis [32, 40–42]. We demonstrate here that the data obtained from our SAXS experiments showing particularly well-defined oscillations at high scattering vectors q, allows us to reliably determine the more complex structure of the pores and distinguish it from a simple cylinder. We have developed a form-factor model that describes the cylindrical nanopores with tapered ends towards the membrane surfaces as observed earlier [14,26–31] and consistent with SEM analysis.

Reliably determining the pore structure is essential for the exploitation of track-etched membranes in advanced applications. Track-etched polycarbonate membranes are widely available as commercial products. They are used for size-selective filtration and separation in medical and biochemical applications [43–49], biological and chemical sensors [50–64], electrophoresis [65], optical sensors [66], and templates for the growth of hydrogels and nanowires of metals, semiconductors, and insulators [27,67–75]. Most of these applications are linked to the transport properties of various particles (ions, molecules, cells, etc.) through the pores. Hence the quantification of the tapered structure presented in this study will directly influence future studies involving track-etched polycarbonate membranes. P. Ramírez et al. [76] have shown, using theoretical models employing a continuum approach based on Nernst-Plank equations, that the transport properties such as conductance, I–V characteristics, rectification ratio, and ion/molecular selectivity through the nanopores are mainly dictated by the shape of the opening of the nanopore. The pore shape, size and size distribution influences the ionic current rectification, electroosmotic flow rectification and the permeability properties of the membrane [49,76–79] and also impact the fluid flow through the pores [80]. Our results quantify the dimensions of the nanopore opening, which is consistent with a truncated cone, and estimate the influence on the transport properties of water in comparison to cylindrical pores. Our results also allow for a better fabrication of single nanopore membranes through careful choice of etching conditions, which are readily utilized for advanced applications, including bio-molecular sensing, DNA sequencing, and water desalination [50,51,56]. Thus, the pore shape quantified in the present study plays a vital role in assessing the properties of and designing new functionalities for track-etched PC membranes.

2. Experimental

2.1. Fabrication of nanopores in PC membranes and SEM characterization

Commercially available polycarbonate POKALON® (LOFO High Tech Films GmbH) films of thickness 20 μm, density 1.2 g cm^{-3}, in the form of circular disks of diameter 50 mm, were irradiated at normal incidence with 2.3 GeV Pb ions at the UNILAC accelerator facility (GSI, Darmstadt, Germany). The average electronic energy loss S_e was calculated using the SRIM2008 code [81] and was found to be 13.7 keV/nm, exhibiting a change of less than 3% across the film thickness ($\Delta S_e \leq 3\%$). The ion fluences ranged from 1×10^8 to 3×10^{10} cm^{-2}. The ion-irradiated samples were exposed to ultraviolet radiation (UV) in air with maximum emission at a wavelength of 315 nm for 1 h from both sides to improve the track to bulk etch ratio. After the UV-sensitization, the samples were etched in 5 M NaOH at 60 °C. Etching times ranged from 60 to 270 s, with an uncertainty of ~1 s. After etching, the samples were rinsed in deionized water and air-dried.

Scanning electron microscopy imaging was performed using a FESEM instrument (Hitachi SU8020, Japan). Before observation, the samples were sputter-coated with an approximately 10 nm thick Au–Pd layer. The specimens were imaged at magnifications that allowed measurement of the pore dimensions. For cross-section imaging, the fracturing technique was used. This involves extensive exposure to ultraviolet light until the specimen becomes sufficiently brittle to break without ductile strain [31]. This procedure made it possible to image the inner structure of the fabricated membranes. However, the long UV exposure of polycarbonate causes ablation (evaporation) of a thin

surface layer. This effect, even being small, can alter the geometry of the nanopores near the foil surface when visualized by SEM. We note that due to the flexible nature of the polymer, this procedure is necessary to achieve meaningful cross-sectional SEM images. To make the membrane brittle and at the same time prevent much alteration of the pore geometry, the UV exposure was performed through 5 μm thick protective PC. The samples used for small angle X-ray scattering, however, did not undergo extensive exposure to ultraviolet light and hence the geometry was not at all affected.

2.2. Small angle X-ray scattering experiments

Transmission SAXS measurements were performed at the SAXS/WAXS beamline at the Australian Synchrotron, using X-rays of energy 12 keV corresponding to a wavelength of 1.03 Å. The distance between the sample and the detector was 7638 mm. Samples were mounted on a three-axis goniometer to enable the alignment of etched tracks with respect to the X-ray beam. Fig. 1(a) and (b) show schematics of the SAXS experimental setup. Data acquisition was performed by first aligning the nanopore axis with the incoming X-ray beam and then taking measurements with the sample tilted by approximately 5° and 10° off the normal. The images produced by the detector correspond to a two-dimensional cut of the pores in reciprocal space [33–36]. When the axis of the pores is almost aligned with the incoming X-ray beam, the SAXS image shows a near-circular-symmetric pattern. An example for a membrane irradiated with a fluence of 1×10^9 ions cm^{-2} and etched for 60 s is shown in Fig. 2(a).

Fig. 2 (b) and (c) show the scattering patterns observed for samples tilted by an angle of 10° for the case of membranes irradiated with a fluence of 1×10^9 ions cm^{-2} and etched for 60 s (b) and irradiated with a fluence of 1×10^8 ions cm^{-2} and etched for 270 s (c). The two-dimensional scattering image exhibits a highly anisotropic pattern resembling narrow curved streaks that result from the high aspect ratio of the pores. The streaks clearly show an oscillating intensity, which contains information about the shape and size of the pore. For analysis, we reduce the two-dimensional scattering image to a one-dimensional scattering intensity by performing an azimuthal integration along the streak using a narrow mask followed by background subtraction using an area away from the streak [82]. Following data reduction, a theoretical model is used to fit the 1D scattering data.

2.3. SAXS modelling

Generally, the SAXS intensity can be divided into two factors. The first factor results from the geometric shape of the scatterers (nanopores) and is called the form factor $f(\vec{q})$ where the scattering vector $\vec{q}$ represents the momentum transfer between the incoming and outgoing waves, with wave vectors, $\vec{k_i}$ and $\vec{k_s}$ respectively,

$$\vec{q} = \vec{k_i} - \vec{k_s} \quad with \quad |\vec{q}| = \frac{4\pi \sin\theta}{\lambda} \tag{1}$$

where λ is the wavelength of the incoming X-ray beam. The angle between the wavevectors of the incoming and scattered beams is 2θ. The second factor results from inter-particle scattering and is called the structure factor $S(\vec{q})$. The net scattering intensity can be written as [33,34],

$$I(\vec{q}) = C\left[f(\vec{q})^2 S(\vec{q}) + f^2(\vec{q}) - f(\vec{q})^2\right] \tag{2}$$

The term $f^2(\vec{q}) - f(\vec{q})^2$ is called Laue scattering and is the contribution from time-dependent systems. In our case, the scattering is independent of time, and thus this term can be neglected. The prefactor C contains the information about the number density of the scatterers and intensity calibration and is considered as a scaling factor in the fitting process. Due to the stochastic nature of the ion irradiation, the nanopores are randomly distributed within the sample with average distances far greater than the track diameter. Hence, the inter-pore scattering is negligible, which leads to the reduction of the structure factor to 1, and the scattering intensity for randomly distributed nanopores can thus be written as

$$I(\vec{q}) = C|f(\vec{q})|^2 \tag{3}$$

The scattering form factor $f(\vec{q})$ is obtained by performing a Fourier transform of the scattering object:

$$f(\vec{q}) = \iiint_V \Delta\rho(\vec{r}) e^{i\vec{q}\cdot\vec{r}} d^3\vec{r} \tag{4}$$

where $\Delta\rho(\vec{r})$ is the function describing the electron density change from the scatterer to the matrix and is defined by the shape, size and density of the scatterer. The nanopores are parallel to each other and are rotationally symmetric around the pore axis. To model the pore, we assume translational symmetry along the pore axis, leading to $\Delta\rho(\vec{r}) = \Delta\rho(r)$. While the translational symmetry is not strictly true for tapered pores, we describe the tapered part of the pores by a radial density variation (as outlined below). The scattering vector $\vec{q}$ and the position vector $\vec{r}$ can conveniently be expressed in cylindrical coordinates (considering the z-axis along the axis of the nanopore) for the given geometry: $\vec{q} = q_r \cos\vartheta\hat{i} + q_r \sin\vartheta\hat{j} + q_z\hat{k}$ and $\vec{r} = r\cos\phi\hat{i} + r\sin\phi\hat{j} + z\hat{k}$ such that $q_r = \sqrt{q_x^2 + q_y^2}$. The scattering form factor can then be written as,

$$f(\vec{q}) = \int_{-\frac{L}{2}}^{\frac{L}{2}} \int_0^{2\pi} \int_0^{\infty} \Delta\rho(r) e^{i\vec{q}\cdot\vec{r}} r dr d\varphi dz \tag{5}$$

where L denotes the length of the nanopores given by the thickness of the membrane. By solving the first two integrals, this can be reduced to:

$$f(\vec{q}) = 2\pi \frac{\sin(q_z L/2)}{q_z/2} \int_0^{\infty} r\Delta\rho(r) J_0(q_r r) dr \tag{6}$$

where J_0 is the Bessel function of zero-order. For simplicity, q_z and q_r can be expressed in terms of $q = |\vec{q}|$, using the geometry displayed in Fig. 1 (c):

$$q_z = q\sin\theta = \frac{q^2\lambda}{4\pi}$$

$$q_r = q\cos\theta = q\sqrt{1 - \left(\frac{q\lambda}{4\pi}\right)^2} \tag{7}$$

Considering the half-length of the nanopore $l = L/2$, Eq. (6) reduces to,

$$f(\vec{q}) = 2\pi \frac{\sin(q\sin(\theta)l)}{q\sin(\theta)/2} \int_0^{\infty} r\Delta\rho(r) J_0(q\cos(\theta)r) dr \tag{8}$$

To model the scattering from cylindrical pores with tapered ends towards the surfaces as suggested by earlier studies, we developed a new form factor that we will refer to as the "Core Taper Model." Fig. 3 illustrates the relation between the pore geometry and the electron density distribution for the Core Taper Model. The respective parameters representing the inner radius of the pore (R_c), the length of the taper region (L_t) and the conical openings at both pore ends are also shown. The core region of the nanopore (R_c) is hollow and represented by a constant electron density change ρ_c. The taper region of the nanopore (T_s) is modelled by a region of increasing electron density denoted as the transition region, where the electron density increases linearly from ρ_c to ρ_s. The parameter ρ_s defines the cutoff value of the density change of

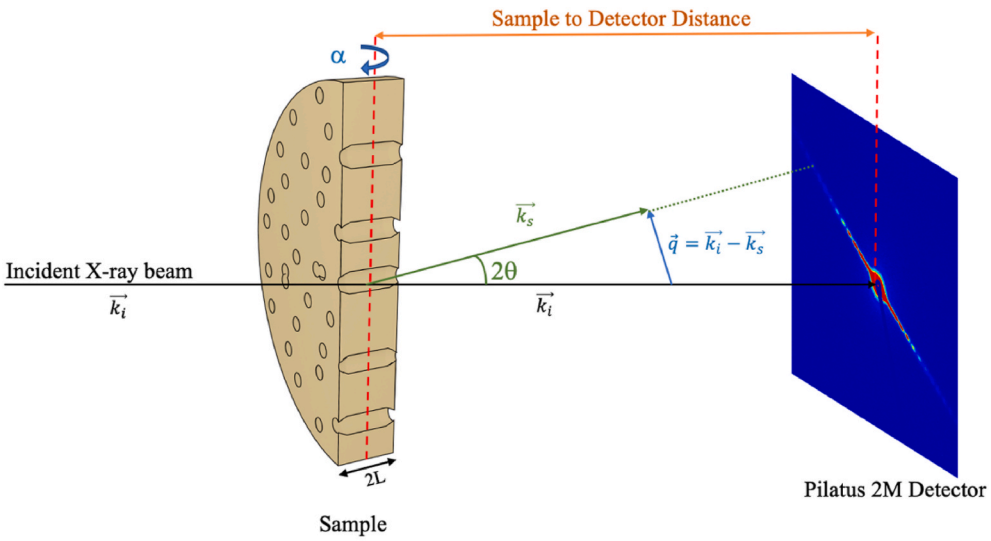

(a)

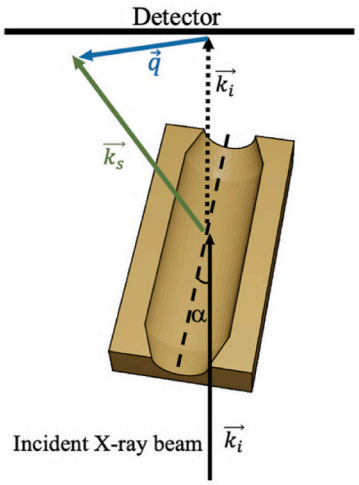

(b)

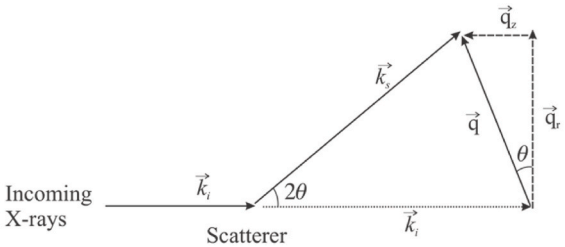

(c)

Figure 1. (a) Side view and (b) top view showing the setup for the small-angle X-ray scattering experiment. The sample is mounted on a three-axis goniometer. The incoming X-ray beam with wave vector $\vec{k_i}$ is scattered from nanopores placed at an arbitrary position $\vec{r}$ and the scattered X-rays with wave vector $\vec{k_s}$ and scattering vector $\vec{q}$ is detected. For our experiments, the sample is tilted at an angle α of approximately 5° and 10° with respect to the incoming X-ray beam. Figure (c) showing the relationship between qz, qr and q.

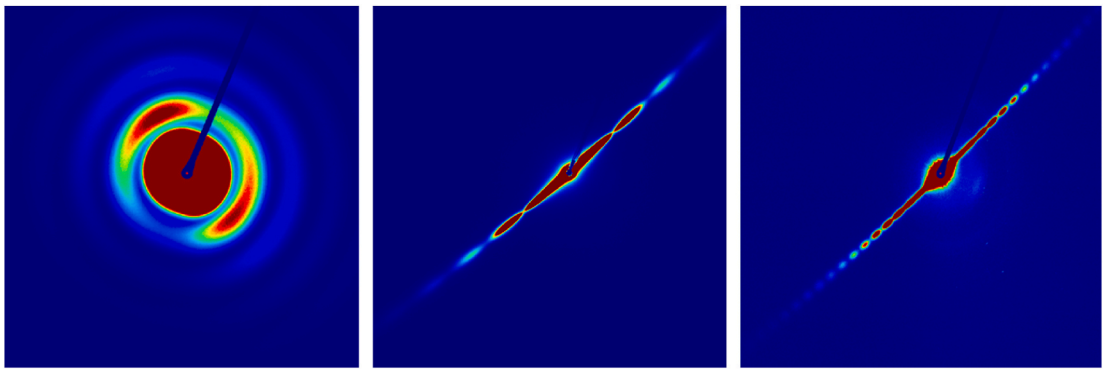

(a) (b) (c)

Fig. 2. Detector images (2D scattering patterns) of PC membranes with parallel oriented nanopores: pore axis aligned to X-ray beam (a), and samples titled by an angle of 10° with respect to the X-ray beam for a membrane irradiated with a fluence of 1×10^9 ions cm^{-2} and etched for 60 s (b) and a membrane irradiated with a fluence of 1×10^8 ions cm^{-2} and etched for 270 s (c). The central part of the detector is protected against the primary beam by a beam stop.

the transition region.

The core region defines the surface radius of the pore, while the transition region with the density change varying from ρ_c to ρ_s defines the tapered section. The transition region is modelled by a linear density increase (using a straight line, see Fig. 3). The slope of the line (m) and y-intercept (c) are given by:

$$m = \frac{\rho_s - \rho_c}{T_s - R_c} \quad and \quad c = \rho_c - mR_c = \frac{\rho_s - \rho_c T_s}{R_c - T_s} \tag{9}$$

The density profile for the Core Taper Model can then be written as:

$$\Delta\rho(r) = \begin{cases} \rho_c & 0 < r \le R_c \\ \left(\frac{\rho_s - \rho_c}{T_s - R_c}\right) r + \frac{\rho_s R_c - \rho_c T_s}{R_c - T_s} & R_c < r \le T_s \\ 0 & T_s < r \end{cases} \tag{10}$$

Solving Eq. (8) using values from Eq. (10), we get

$$f(\vec{q}) = 2\pi \frac{sin(q_z l)}{q_z/2} \frac{(\rho_s - \rho_c)}{q_r^3 (T_s - R_c)} \Big(- q_r^2 R_c^2 J_1(q_r R_c) + q_r^2 T_s^2 J_1(q_r T_s) + \frac{1}{2}\pi q_r R_c (H_0(q_r R_c) J_1(q_r R_c) - H_1(q_r R_c) J_0(q_r R_c)) - \frac{1}{2}\pi q_r T_s (H_0(q_r T_s) J_1(q_r T_s) - H_1(q_r T_s) J_0(q_r T_s)) \Big) - \frac{(\rho_s R_c - \rho_c T_s)(R_c J_1(q_r R_c) - T_s J_1(q_r T_s))}{q_r (R_c - T_s)} + \frac{\rho_c R_c J_1(q_r R_c)}{q_r} \tag{11}$$

where J_1 is the Bessel function of first-order and $H_v(z)$ is the Struve function defined as:

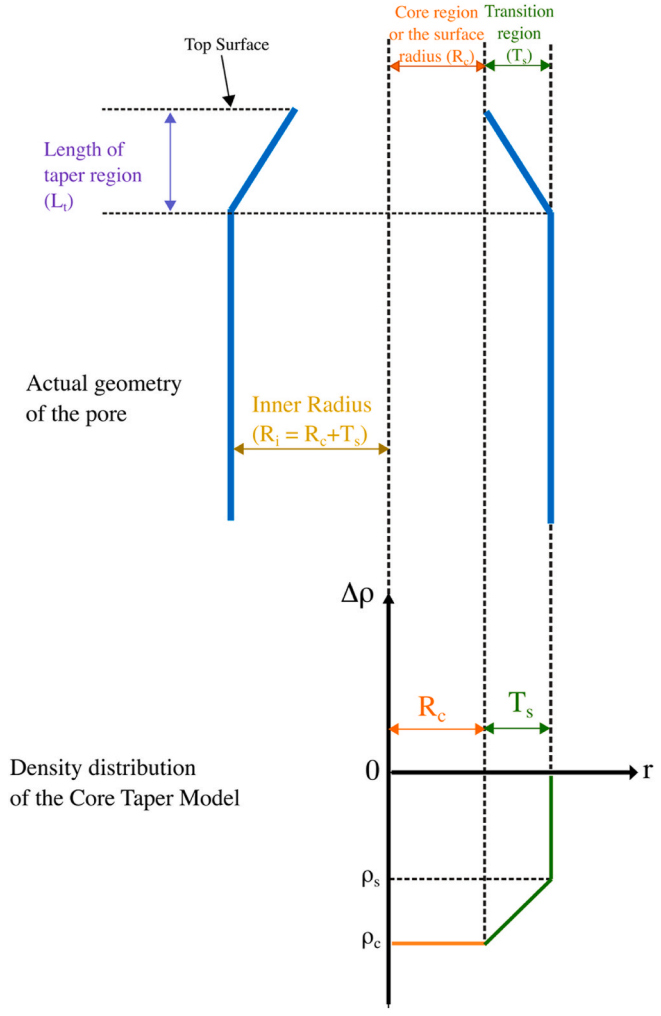

Fig. 3. Graphical representation showing the relation between the radial electron density profile for the Core Taper Model (bottom) and the actual geometry of the pore (top). Only the top half of the pore is shown for easy visualisation.

$$H_v(z) = \left(\frac{1}{2}z\right)^{v+1} \sum_{k=0}^{\infty} \frac{(-1)^k \left(\frac{1}{2}z\right)^{2k}}{\Gamma\left(k + \frac{3}{2}\right)\Gamma\left(k + v + \frac{3}{2}\right)}$$

The constant density change of the core (ρ_c) can be set to -1, such that the fitting parameter ρ_s will be normalised to ρ_c. This is done to eliminate one fitting parameter and thus reduce the complexity of the fit function. This leads to:

$$f(\vec{q}) = 2\pi \frac{sin(q_z l)}{q_z/2} \frac{1}{2q_r^2} \frac{1}{R_c - T_s} \pi(\rho_s + 1)(- R_c H_0(q_r R_c) J_1(q_r R_c) + R_c H_1(q_r R_c) J_0(q_r R_c) + T_s H_0(q_r T_s) J_1(q_r T_s) - T_s H_1(q_r T_s) J_0(q_r T_s)) + 2\rho_s q_r T_s J_1(q_r T_s) \tag{12}$$

In practice, not all pores have exactly the same radius. We take this into account by implementing a narrow Schulz-Zimm distribution [41, 82]. which is very similar to a Gaussian distribution for small values of the dispersity. It has the advantage that non-physical negative radii cannot contribute to the average. The standard deviation or the width of the distribution defines the dispersity in the radius values. With this modification, the scattering intensity can be written as,

$$I(\vec{q}) = C \int_0^{\infty} p(R_0, R) dR |f(\vec{q}, R, L)|^2 \tag{13}$$

with,

$$p(R_0, R) = \frac{1}{Norm} (z+1)^{z+1} \left(\frac{R}{R_0}\right)^z \frac{exp(-(z+1)R/R_0)}{R_0 \Gamma(z+1)}$$

Norm is the normalization factor. The variable z defines the width of the distribution:

$$z = \frac{1 - \sigma^2}{\sigma^2}$$

where σ is the dispersity parameter used in the fitting model given by:

$$\sigma = \frac{p}{\bar{x}}$$

where $\bar{x}$ is the mean of the distribution (in our case $\bar{x}$ is the radius) and p is the root mean square deviation from $\bar{x}$. The size distribution of the

transition region T_s with a mean value of t_S is fixed by scaling the distribution applied on R_c to t_s/R_0. While deriving the scattering form-factor (Eq. (12)), we have considered that all the nanopores are parallel to each other, but in reality, this is not the case. This deviation is due to the small ion-beam divergence during irradiation and because the membranes may not be entirely flat during the SAXS measurements. To account for this, we implement a small box angular distribution, with ω being used as a fit parameter:

$$I'(\vec{q}) = \frac{\int_{-\omega}^{\omega} I(\vec{q})\sin\theta d\theta}{\int_{-\omega}^{\omega} \sin\theta d\theta} \tag{14}$$

Here $I'(\vec{q})$ defines the scattering intensity resulting from angularly distributed scatterers, with small angular dispersion ω. In summary, the scattering intensity from the nanopores defined using our Core Taper Model is given as:

$$I'(\vec{q}) = \frac{C}{\int_0^{\omega} \sin\theta d\theta} \int_0^{\omega} \int_0^{\infty} |f(\vec{q})|^2 p(R_c, R_0) dR_c \sin\theta d\theta + I_{bkg} \tag{15}$$

where the term I_{bkg} is included to account for a constant background.

3. Results and discussion

The fitting of the 1D SAXS data obtained after data reduction was performed using a Python and C-based code implementing a non-linear least-square fitting algorithm [83]. After reducing the data, well-defined oscillations are observed for all samples. For samples exposed to the same etching time, the oscillations start to smear out with increasing fluence. This effect directly points towards a broadening of the size distribution of the pores. Also, the oscillations shift to higher q values with increasing fluence indicating a small change of the pore dimensions. Fig. 4 shows the SAXS scattering intensities for samples irradiated with different fluences and etched for 60 s. The arrow in the figure indicates the shift of the oscillations. The smearing of the oscillations is also clearly apparent in Fig. 4. The results indicate that with increasing fluence, the radius of the pores decreases slightly, and the dispersity increases. This effect is also confirmed by the fitting results.

Fig. 5 shows fits to the scattering intensity for a PC membrane irradiated with 1×10^8 ions cm^{-2} and etched for 270 s using both, the Core Taper Model and the simple Hard Cylinder Model. The Hard Cylinder Model assumes the nanopores to be cylindrical in shape and is defined by a step like electron density change [41,42,84]. As is evident from the figure, the Core Taper Model gives a much better fit to the data than the Hard Cylinder Model, in particular for high q-values. A small chirp in the oscillations is observed in the experimental data when compared to the Hard Cylinder fit with increasing q-values. In contrast, the Core Taper Model reproduces the data extremely well over the entire q-range. Only high-quality scattering data with many oscillations allows to distinguish between the two models and yields more detailed information about the shape and size of the pores. The Hard-Cylinder model generally gives a very good approximation to the pore size, yet details of the structure may not be resolved.

The reduced scattering intensities obtained for membranes etched for different times, along with their numerical fit curves using the Core Taper Model, are shown in Fig. 6. The fits reproduce the data with great accuracy. The information on the track morphology for all the samples is summarized in Table 1. The surface radius values obtained from the

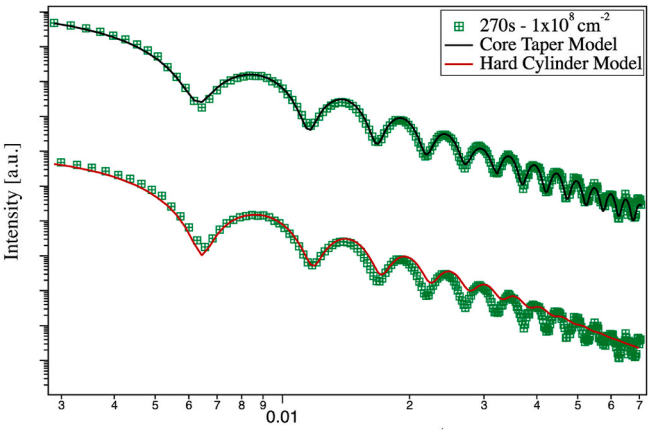

Fig. 5. Integrated SAXS scattering intensities for a PC membrane irradiated with 1×10^8 ions cm^{-2} and etched for 270 s. The solid lines represent the numerical fit using the Core Taper Model (black) and the Hard Cylinder Model (red). The scattering oscillations at higher q values fit significantly better using the Core Taper Model compared to the Hard Cylinder Model. (For interpretation of the references to colour in this figure legend, the reader is referred to the Web version of this article.)

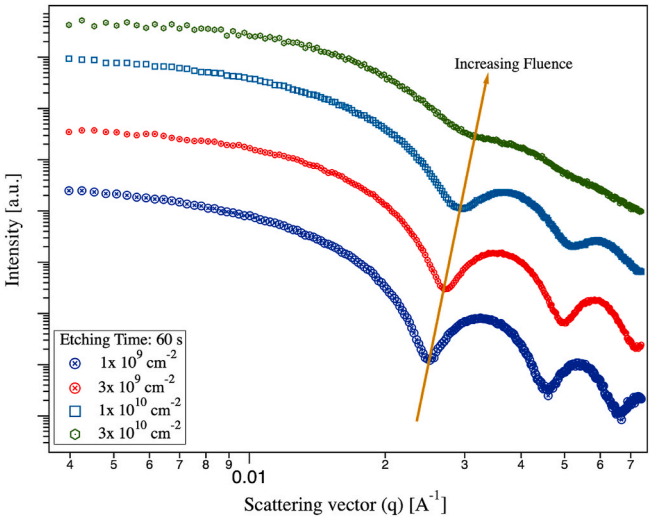

Fig. 4. Integrated SAXS scattering intensities for PC samples irradiated with different fluences and etched for 60 s (5 M NaOH at 60 °C). The shift in the oscillations of the scattering intensities is due to a decrease in pore radius with increasing fluence. The smearing out of the oscillations indicates increasing dispersity for higher fluences. The patterns are stacked for better visibility.

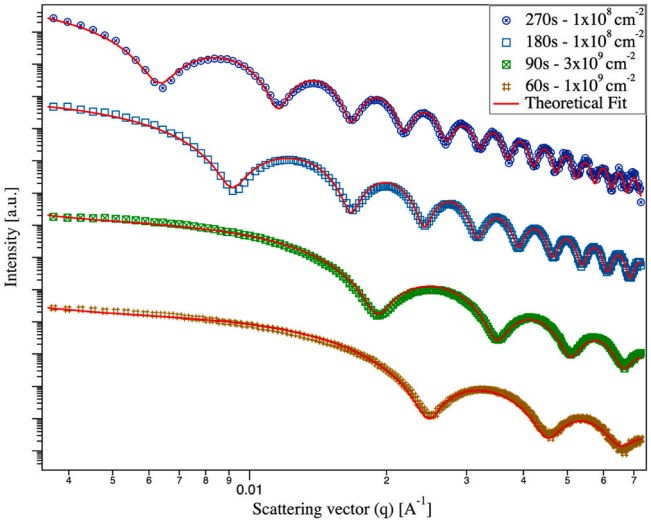

Fig. 6. Integrated SAXS scattering intensities for samples etched for different times. The solid red lines represent the numerical fits obtained using the Core Taper Model. (For interpretation of the references to colour in this figure legend, the reader is referred to the Web version of this article.)

SAXS fits will give the radius of the pore as measured from the plan-view SEM images. The transition region value defines the width of the taper part, and the length of the taper part is deduced from the values of ρ_s. The sum of the surface radius and transition region represents the radius of the inner cylindrical part of the pore. The overlap is considered as the percentage of the pores overlapping per transformed area during the ion-irradiation with fluence F and has been calculated using an overlap model $A = 1 - \exp(-\pi R^2 F)$, as explained in C. Riedel et al. [85].

Fig. 7 shows a graphical representation of the evolution of the pores with increasing etch time. Once the taper structure of the nanopores is formed, the width and length of the taper region remain almost unchanged, indicating the origin of the structure to be related to the early evolution of the pore. SEM images of PC membranes irradiated with different fluences and etched for different times are shown in Fig. 8. Fig. 8(a), (b) and (c) shows the plan-view SEM images of PC membranes irradiated with 1×10^{10} ions cm^{-2}, 1×10^{9} ions cm^{-2}, and 3×10^{8} ions cm^{-2} and etched for 90 s, 180 s and 270 s respectively. Fig. 8(d) and (e) show the cross-section SEM images of PC membranes irradiated 3×10^{8} ions cm^{-2} and etched for 210 s towards the top surface and bottom surface of the membrane respectively. The taper region is clearly visible in the cross-section images and in good agreement with the dimensions obtained from SAXS measurements. We measured the radii from the plan-view SEM images of selected membranes. Within the uncertainties, all SEM values (except the one etched for 270s with a fluence of 3×10^{8}) agree well with the surface radius values from fit results. The discrepancy may be caused by the metal coating done for SEM imaging. The values obtained from the SEM and SAXS measurements are compared in Table 2.

The influence of the pore shape can be estimated by calculating the flow of viscous liquid through a cylindrical nanopore and a tapered nanopore. Let us consider a tapered nanopore with total length L, surface radius R_c, inner radius R_i, and length of the taper region L_t as shown in Fig. 3. The flow of a liquid with dynamic viscosity μ through the cylindrical part of the pore is described by the Poiseuille law [86]:

$$P_{cyl} = \frac{8\mu(L-2L_t)Q}{\pi R_i^4} \tag{16}$$

where P_{cyl} is the pressure drop, $L - 2L_t$ is the length of the cylindrical part of the pore with radius R_i and Q is the volumetric flow rate. The pressure drop P_{tap} across the tapered region of the nanopore at the same volumetric flow rate is given by [87]:

$$P_{tap} = \frac{8\mu L_t Q}{3\pi R_c^4}\left(\left(\frac{R_c}{R_i}\right) + \left(\frac{R_c}{R_i}\right)^2 + \left(\frac{R_c}{R_i}\right)^3\right) \tag{17}$$

This equation is valid for small cone angles which is applicable for our case as the length of the taper region is significantly larger than the surface radius ($L_t \gg R_c$). The pressure drop across the whole pore channel is then $P = P_{cyl} + 2P_{tap}$. Using this, the volumetric flow rate through the nanopore with tapered ends can be calculated as:

$$Q = \frac{\pi P}{8\mu\left(\frac{2L_t f}{3R_c^4} + \frac{L-2L_t}{R_i^4}\right)} \tag{18}$$

where $f = \left(\frac{R_c}{R_i}\right) + \left(\frac{R_c}{R_i}\right)^2 + \left(\frac{R_c}{R_i}\right)^3$. It should be noted that equations (16)–(18) do not take into account the end effects, i.e., the losses for viscous friction outside the pore channel at the entrance and the exit. In

Table 1
Fitting parameters from SAXS measurements for different samples using the Core Taper Model: R_c (Surface radius), T_s (Transition region), R_i (Inner radius = $R_c + T_s$), L_t (length of taper region). The term ρ_s defines the cutoff value of the density change of the transition region and is normalised to the core density change ρ_c. The absolute dispersity and relative dispersity normalised to R_c has been given. The overlap has been calculated using an overlap model explained in Ref. [85].

Sample Information		Morphology of the track							
Etching time (s)	Fluence (ions cm^{-2})	Surface radius R_c (nm)	Transition Region T_s(nm)	Inner Radius R_i(nm)	ρ_s	Length of taper region L_t(μm)	Dispersity		Overlap (%)
							nm	percentage	
60	1×10^{9}	9.1 ± 0.3	8.1 ± 0.4	17.2 ± 0.7	−0.84 ± 0.03	1.6 ± 0.1	0.5 ± 0.01	5.7% ± 0.2%	0.1%
60	3×10^{9}	8.4 ± 0.3	7.9 ± 0.5	16.3 ± 0.8	−0.83 ± 0.03	1.7 ± 0.1	0.5 ± 0.03	6.1% ± 0.3%	0.4%
60	1×10^{10}	8.0 ± 0.3	7.6 ± 0.7	15.6 ± 1.0	−0.83 ± 0.03	1.7 ± 0.1	0.8 ± 0.03	9.1% ± 0.4%	1.3%
60	3×10^{10}	7.6 ± 0.7	7.3 ± 0.9	14.9 ± 1.6	−0.82 ± 0.03	1.8 ± 0.1	1.5 ± 0.03	19.2% ± 0.4%	2.4%
90	3×10^{9}	14.1 ± 0.2	8.3 ± 0.4	22.4 ± 0.6	−0.84 ± 0.03	1.6 ± 0.1	0.8 ± 0.01	5.3% ± 0.1%	0.9%
90	1×10^{10}	13.8 ± 0.4	7.9 ± 0.5	21.7 ± 0.9	−0.83 ± 0.04	1.7 ± 0.1	1.4 ± 0.04	10.1% ± 0.3%	3.1%
90	3×10^{10}	13.4 ± 0.5	7.4 ± 0.6	20.8 ± 1.1	−0.83 ± 0.04	1.7 ± 0.1	2.6 ± 0.08	18.9% ± 0.6%	9.5%
180	1×10^{8}	33.6 ± 0.3	8.3 ± 0.4	41.9 ± 0.7	−0.85 ± 0.03	1.5 ± 0.1	1.3 ± 0.06	4.0% ± 0.2%	0.2%
180	3×10^{8}	33.5 ± 0.4	8.3 ± 0.7	41.8 ± 1.1	−0.85 ± 0.03	1.5 ± 0.1	1.3 ± 0.03	3.9% ± 0.1%	0.5%
180	1×10^{9}	33.2 ± 0.5	8.2 ± 0.4	41.4 ± 0.9	−0.85 ± 0.02	1.5 ± 0.1	1.4 ± 0.07	4.1% ± 0.2%	1.7%
180	3×10^{9}	32.3 ± 0.5	8.1 ± 0.5	40.4 ± 1.0	−0.84 ± 0.03	1.6 ± 0.1	1.9 ± 0.13	5.9% ± 0.4%	5.2%
180	1×10^{10}	31.7 ± 0.6	7.7 ± 0.7	39.4 ± 1.3	−0.84 ± 0.04	1.6 ± 0.1	3.0 ± 0.11	9.5% ± 0.3%	18.1%
270	1×10^{8}	52.5 ± 0.3	8.5 ± 0.3	61.0 ± 0.6	−0.86 ± 0.03	1.4 ± 0.1	2.2 ± 0.1	4.2% ± 0.2%	0.5%
270	3×10^{8}	52.4 ± 0.4	8.6 ± 0.2	61.0 ± 0.6	−0.85 ± 0.02	1.5 ± 0.1	2.1 ± 0.1	4.1% ± 0.2%	1.3%
270	1×10^{9}	52.5 ± 0.4	8.4 ± 0.3	61.0 ± 0.7	−0.85 ± 0.04	1.5 ± 0.1	2.2 ± 0.1	4.1% ± 0.2%	4.5%

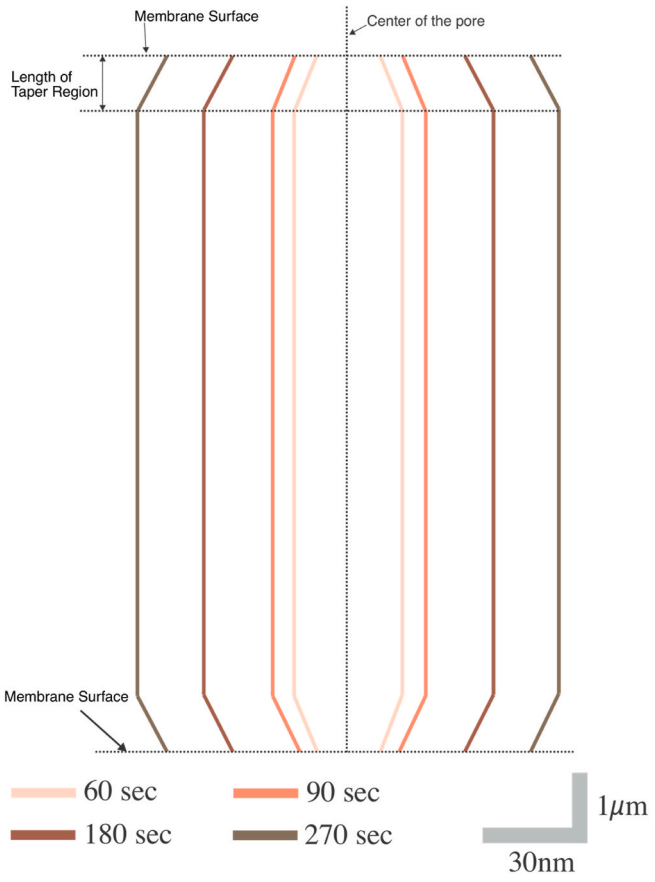

Fig. 7. Graphical representation (length and width are drawn on different scales for easy visualisation) of the evolution of the pores with increasing etch time.

our case the end effects are negligible because $L_t \gg R_c$. We are also not considering the overlap of nanopores and the effects of surface charge on the flow of ions/molecules through the nanopores for these calculations.

The deviation of the nanopore shape from an ideal cylinder should be taken into account when track-etched polycarbonate membranes are used in high precision electrokinetic or nanofluidic experiments. Using equation (18), we calculate the water flow rates through the tapered pore channels with different R_i, R_c, L_t values as determined from SAXS in the present study. For comparison, we have calculated the water flow rates for cylindrical nanopores as well where the nanopore radius was chosen as the surface pore radius, which can be determined by plan-view SEM. The water flow rates for both the cases are listed in Table 3. From the data as shown in Table 3, it is apparent, that there is a significant difference between the two flow rates, which increases with decreasing pore size. An experimentalist who determines the transport characteristics of membranes in a liquid will need to take into account the full geometry to match their results with appropriate calculation. Such situations were described in references [14,26,27]. The difference will become even greater for membranes with a smaller thickness where the difference between L and L_t is not large [31]. Accounting for the real geometry of pore channels allows resolving the contradiction between the different methods of membrane characterization. It should be noted that the effect of non-cylindrical pore shape is particularly important when PC membranes with small nanopores are used for filtration of liquids. In the case of gases, the pressure-driven flow through nanochannels is proportional to the 3rd power of the pore radius (the Knudsen flow [88]), and therefore the effect of pore geometry is not as strong as in the case of the Poiseuille flow.

Fig. 9 (a) shows the surface radius derived from SAXS and measured from the plan-view SEM images as a function of fluence. The surface radius remains almost constant up to a fluence of 1×10^9 ions/cm^2, after which it decreases slightly. This fluence effect was discussed earlier and is consistent with the change of the position of the oscillations observed in the one-dimensional scattering data (Fig. 4). Fig. 9 (b) shows the inner radius derived from SAXS with increasing fluence, which shows similar behavior to the surface radius. Also, with increasing fluence, the dispersity significantly increases, in particular when the fluence exceeds 1×10^9 ions/cm^2. This behavior is shown in Fig. 10. The increase in dispersity can be explained by the combined effect of the increasing overlap of the halo region (explained below) and increasing overlap of the etched region with increasing fluence. The relative dispersity normalised to the core radius as a function of etching time, however, remains almost the same, which indicates that the size distribution in the pores is either caused by variations from track to track or originates from variations in the early stages of etching and once the structure of the nanopores is well formed, it remains constant.

Fig. 11 shows the surface radius (a) and the inner radius (b) as a function of etching time for different fluences. The pore size increases linearly with the etching time. The linear fits to the data give us the radial etch rate for each fluence (Table 4). The radial etch-rates deduced from our measurements agree very well with the radial etch rate of 12 nm/min obtained by G. Pépy et al. [40] in PC membranes irradiated with 1.4 GeV Xe ions (fluence $= 3 \times 10^8, 5 \times 10^8$, and 1×10^9 ions cm^{-2}) and etched under the same conditions, i.e. using 5 M NaOH solution at 60 °C.

The highest etch rates for surface and inner radius is found to be 12.6 ± 0.3 nm/min and 12.8 ± 0.6 nm/min, respectively, for membranes irradiated with 1×10^8 ions cm^{-2} which reduces to 11.6 ± 1.5 nm/min and 11.8 ± 2.1 nm/min, respectively, for membranes irradiated with 3×10^{10} ions cm^{-2}. This slight decrease in the etch rates is also confirmed by the fact that both surface and inner radii consistently decrease for membranes irradiated with fluences higher than 1×10^9 ions cm^{-2} (Table 4). N. Sertova et al. [89] investigated the track etching behavior of PC foils irradiated with Pb and Ca ions and also found that the radial etch rate decreases with increasing fluence.

Based on the experimental results available so far [89–93], this change in etch rate is probably caused by the track halo around the track core. Tracks in polymers are typically described by two regions, the track core and the track halo. In the track core, the material is severely damaged and characterized by bond breaking and outgassing of volatile degradation products. The halo region around the core is ascribed mainly to the electron cascade initiated by the projectile ion. The dose deposition in this radial halo region is less than in the core and decreases radially. By conductometric measurements, a reduced radial etch rate was observed in the halo region of some polymers, and this higher resistance to chemical etching as compared to the matrix was ascribed to cross-linking [90–92]. With increasing fluence, the average distance between neighbouring halos becomes smaller and smaller. When two neighbouring halos overlap, an increase in the amount of cross-linking is expected. This may affect the etching process and explain our observation that at fluences above 1×10^9 ions cm^{-2}, the etching rate decreases slightly. The increase in dispersity above the fluence of 1×10^9 ions cm^{-2} is independent of the etching time. This indicates that pore overlap cannot be the sole reason for observed decrease in etching rate. We have previously observed that the small-angle scattering from tracks and

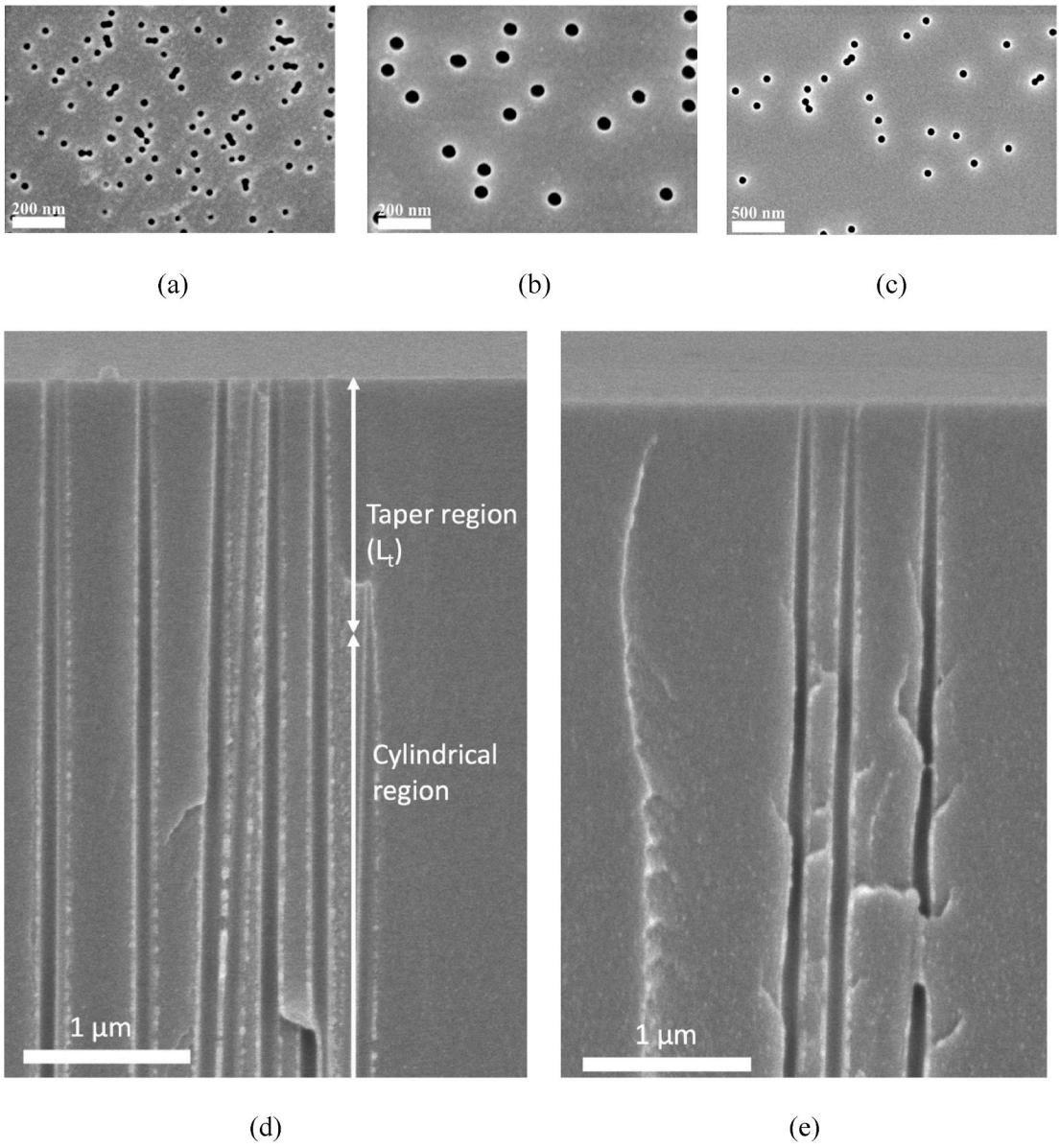

Fig. 8. SEM images of nanopores fabricated in PC membranes irradiated with different fluences and etched for different times in 5 M NaOH at 60 °C (a) plan-view with a fluence of 1×10^{10} ions cm-2 and etched for 90 s. (b) plan-view with a fluence of 1×10^{9} ions cm-2 and etched for 180 s. (c) plan-view with a fluence of 3×10^{8} ions cm-2 and etched for 270 s. Cross-section SEM towards top surface (d) and bottom surface (e) of the membrane irradiated with a fluence of 3×10^{8} and etched for 210 s. Taper region and cylindrical region are indicated in (d).

pores is affected when the track/pore overlap exceeds approximately 20% [94,95]. If we assume that the radial etch rate decreases when ~20% overlap of the halos is reached, the radius of the relevant halo region is estimated to be about 120 nm. This estimate agrees well with earlier estimated values e.g., by D. Fink [93] who reported the radial extent of the halo region exceeding 100 nm depending on the electronic stopping power of the incoming ion.

4. Conclusions

In this study, we have utilized SAXS measurements in conjunction with SEM to characterize nanopores in PC fabricated by the track-etch technology. We determined the size and shape details of the nanopores as a function of the etching time and irradiation fluence. By implementing a new form-factor model (Core Taper Model) for the fit process of the SAXS data, we suggest a cylindrical interior of the pore that tapers to smaller radii at the polymer surfaces. The surface radius is typically ~8 nm smaller than the radius in the bulk of the polymer foil. This finding is important because the pore size of ion track membranes is generally determined by SEM assuming that the surface and bulk radius is identical. Calculations of the flow rate show that a tapered pore orifice should have a significant impact on the transport, filtration and sensing properties of the membranes. This special surface geometry needs to be

Table 2
Comparison of radii measured by plan-view SEM and surface radius values deduced by fitting SAXS data.

Etching time(s)	Fluence (ions cm^{-2})	Radius values from plan-view SEM (nm)	Surface radius values from SAXS (nm)
90	1×10^{10}	12.9 ± 2.1	13.8 ± 0.4
90	3×10^{10}	12.7 ± 2.4	13.4 ± 0.5
180	1×10^{9}	29.6 ± 3.2	33.2 ± 0.5
180	3×10^{9}	30.2 ± 2.2	32.3 ± 0.5
270	3×10^{8}	41.3 ± 3.5	52.4 ± 0.4

Table 3
Comparison of water flow rates in membranes with tapered and cylindrical nanopores.

Etching time (s)	Pore density (ions cm^{-2})	Surface pore radius R_c (nm)	Inner pore radius R_i (nm)	Length of taper region L_t (μm)	Water flow rate at $P = 1$ bar, $cm^3\ cm^{-2}\ min^{-1}$	Ratio of the flow rates (tapered/ cylindrical)
60	3×10^{10}	7.6	14.9	1.8	0.1073	9.17
	3×10^{10}	Cylinders 7.6 nm in radius			0.0117	
90	3×10^{10}	13.4	20.8	1.7	0.5215	4.59
	3×10^{10}	Cylinders 13.4 nm in radius			0.1137	
180	3×10^{9}	32.3	40.4	1.6	0.8588	2.24
	3×10^{9}	Cylinders 32.3 nm in radius			0.3841	
270	1×10^{9}	52.5	61.0	1.5	1.5451	1.73
	1×10^{9}	Cylinders 52.5 nm in radius			0.8936	

considered when using track-etched PC membranes for different applications.

The exact reason for the specific tapered pore shape in PC is still not fully understood. In the case of commercial membranes, the use of surfactants during etching contributes to the effect of pore taper at both ends. However, the factors such as etchant-induced heterogeneity and the impact of a non-uniform matrix on the nanopore structure may also play an important role [31]. Combining those with the study of the early evolution of pore formation using SAXS can reveal more details about the origin of the observed pore shape.

Our measurements also demonstrate clear effects of the ion fluence. The size distribution of the pores increases, and the pore dimension slightly decreases when the fluence exceeds 1×10^9 ions cm^{-2}. The latter effect is attributed to a halo around the track core which exhibits cross-linking of polymer chains. With increasing fluence, the halo regions overlap, and the increased cross-linking in the overlap areas leads to a reduction in the radial etch rate. The size of the halo region has been approximately determined to be 120 nm.

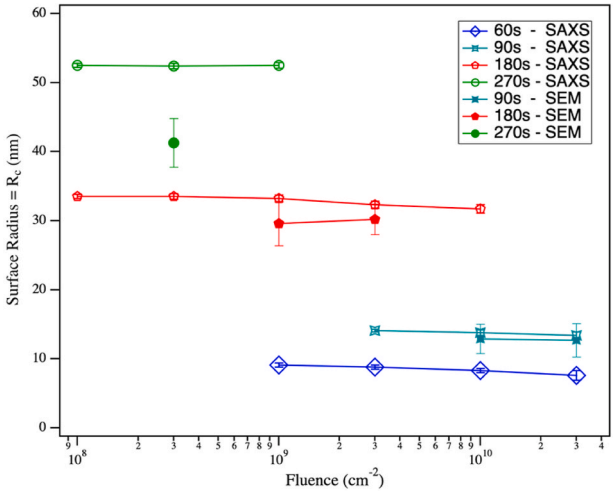

(a)

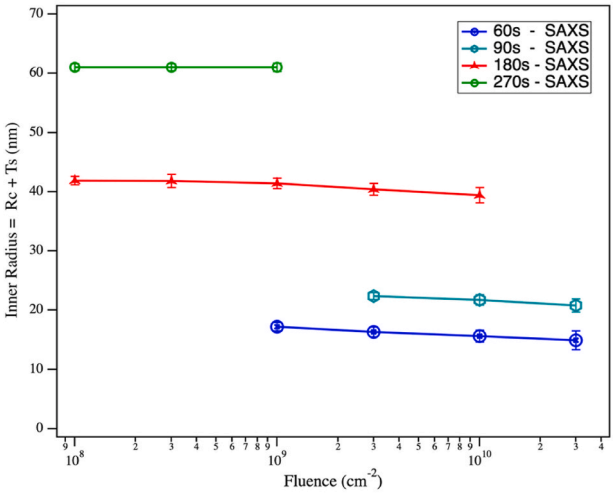

(b)

Fig. 9. Pore radii as a function of fluence (a) radii measured from plan-view SEM and core radii deduced from fits to the SAXS data. (b) Inner pore radii from fitted data using the Core Taper Model. Both surface radii and inner radii remain almost constant up to a fluence of 1×10^9 ions/cm2, and then slightly decrease with increasing fluence.

CRediT authorship contribution statement

Shankar Dutt: Conceptualization, Methodology, Software, Investigation, Formal analysis, Writing – original draft. **Pavel Apel:** Conceptualization, Methodology, Investigation, Writing – review & editing. **Nikolay Lizunov:** Investigation. **Christian Notthoff:** Software. **Qi Wen:** Investigation. **Christina Trautmann:** Investigation, Writing – review & editing. **Pablo Mota-Santiago:** Investigation. **Nigel Kirby:** Investigation. **Patrick Kluth:** Conceptualization, Methodology, Investigation, Writing – review & editing, Supervision.

Declaration of competing interest

The authors declare that they have no known competing financial interests or personal relationships that could have appeared to influence the work reported in this paper.

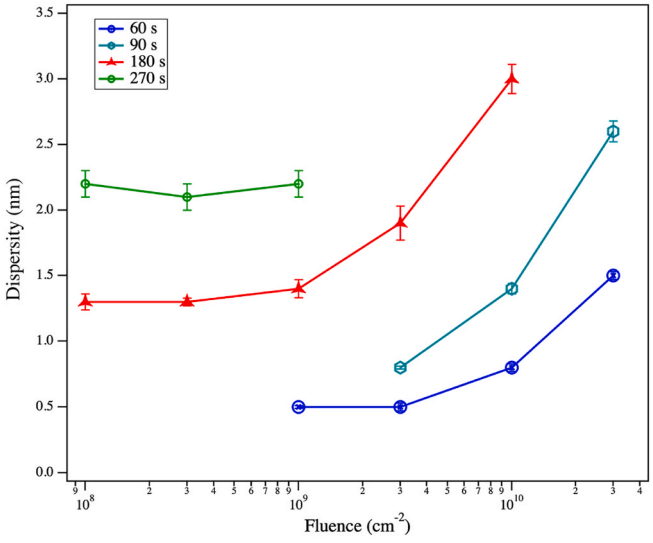

Fig. 10. Size dispersity as a function of fluence for different etching times (nanopore size). The dispersity increases for fluences larger than 1×10^9 ions/cm^2.

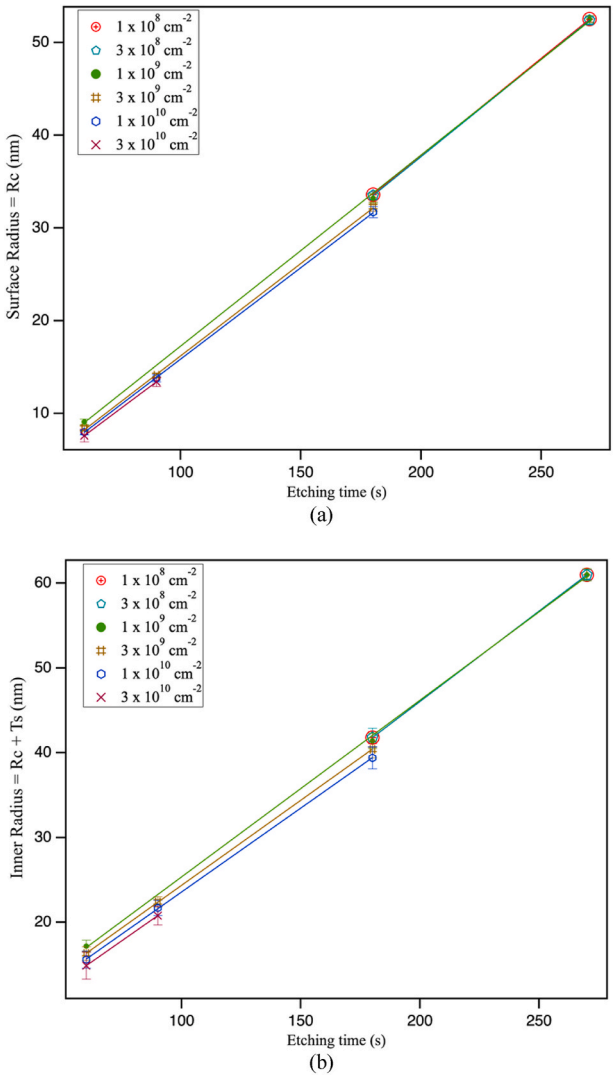

Fig. 11. Nanopore radii as a function of etching time for different fluences, The results are deduced from fits to SAXS data using the Core Taper Model: (a) surface radius and (b) inner radius of nanopores. Linear fits(solid lines) to the data yields radial etch rates.

Table 4
Radial etch rates for different fluences obtained from linear fits to the pore radii as a function of etching time (Fig. 11).

Fluence (ions cm^{-2})	Radial Etch Rate of Surface radius (nm min^{-1})	Radial Etch Rate of Inner Radius (nm min^{-1})
$\mathbf{1 \times 10^8}$	12.6 ± 0.3	12.8 ± 0.6
$\mathbf{3 \times 10^8}$	12.6 ± 0.4	12.8 ± 0.8
$\mathbf{1 \times 10^9}$	12.4 ± 0.2	12.5 ± 0.3
$\mathbf{3 \times 10^9}$	12.0 ± 0.3	12.0 ± 0.6
$\mathbf{1 \times 10^{10}}$	11.8 ± 0.4	11.9 ± 0.8
$\mathbf{3 \times 10^{10}}$	11.6 ± 1.5	11.8 ± 2.1

Acknowledgments

Part of the research was undertaken at the SAXS/WAXS beamline at the Australian Synchrotron, part of ANSTO, and we thank the beamline scientists for their technical assistance. This research was supported by an AINSE Ltd. Postgraduate Research Award (PGRA) and Australian Government Research Training Program (RTP) Scholarship. The authors also acknowledge financial support from the Australian Research Council (ARC) under the ARC Discovery Project Scheme (DP180100068).

References

[1] R.L. Fleischer, P.B. Price, Tracks of charged particles in high polymers, Science 140 (1963) 1221–1222, https://doi.org/10.1126/science.140.3572.1221.
[2] D.M. Karl, Plastics-irradiated-etched: the Nuclepore® fiter turns 45 years old, Limnol. Oceanogr. Bull. 16 (2007) 49–54, https://doi.org/10.1002/lob.200716349.
[3] R.L. Fleischer, Tracks to innovation — interplay between science and technology, Radiat. Meas. 28 (1997) 763–772, https://doi.org/10.1007/978-1-4612-4452-3.
[4] B.E. Fischer, R. Spohr, Production and use of nuclear tracks: imprinting structure on solids, Rev. Mod. Phys. 55 (1983) 907–948. https://doi.org/10.1103/RevModPhys.55.907.
[5] P. Apel, Track etching technique in membrane technology, Radiat. Meas. 34 (2001) 559–566, https://doi.org/10.1016/S1350-4487(01)00228-1.
[6] W.M. Deen, Hindered transport of large molecules in liquid-filled pores, AIChE J. 33 (1987) 1409–1425, https://doi.org/10.1002/aic.690330902.
[7] P. Stroeve, N. Ileri, Biotechnical and other applications of nanoporous membranes, Trends Biotechnol. 29 (2011) 259–266. https://doi.org/10.1016/j.tibtech.2011.02.002.
[8] H. Zhang, Y. Tian, L. Jiang, Fundamental studies and practical applications of bio-inspired smart solid-state nanopores and nanochannels, Nano Today 11 (2016) 61–81. https://doi.org/10.1016/j.nantod.2015.11.001.
[9] F. Liu, M. Wang, X. Wang, P. Wang, W. Shen, S. Ding, Y. Wang, Fabrication and application of nanoporous polymer ion-track membranes, Nanotechnology 30 (2019) 52001. https://doi.org/10.1088/1361-6528/aaed6d.
[10] P.Y. Apel, Fabrication of functional micro- and nanoporous materials from polymers modified by swift heavy ions, Radiat. Phys. Chem. 159 (2019) 25–34. https://doi.org/10.1016/j.radphyschem.2019.01.009.
[11] T. Ma, J. Janot, S. Balme, Track-etched nanopore/membrane: from fundamental to applications, Small Methods 4 (2020) 2000366, https://doi.org/10.1002/smtd.202000366.
[12] C. Wen, S.-L. Zhang, Fundamentals and potentials of solid-state nanopores: a review, J. Phys. Appl. Phys. 54 (2) (2020), https://doi.org/10.1088/1361-6463/ababce, 023001.
[13] P. Meares, K.R. Page, Rapid force-flux transitions in highly porous membranes 272 (1972) 1–46.
[14] D.S. Cannell, F. Rondelez, Diffusion of polystyrenes through microporous membranes, Macromolecules 13 (1980) 1599–1602. https://doi.org/10.1021/ma60078a046.
[15] W.H. Keesom, R.L. Zelenka, C.J. Radke, A zeta-potential model for ionic surfactant adsorption on an ionogenic hydrophobic surface, J. Colloid Interface Sci. 125 (1988) 575–585. https://doi.org/10.1016/0021-9797(88)90024-0.
[16] A.A. Lev, Y.E. Korchev, T.K. Rostovtseva, C.L. Bashford, D.T. Edmonds, C. A. Pasternak, Rapid switching of ion current in narrow pores: implications for biological ion channels, Proc. R. Soc. Lond. B Biol. Sci. 252 (1993) 187–192. https://doi.org/10.1098/rspb.1993.0064.
[17] A. Yaroshchuk, O. Zhukova, M. Ulbricht, V. Ribitsch, Electrochemical and other transport properties of nanoporous track-etched membranes studied by the current switch-off technique, Langmuir 21 (2005) 6872–6882. https://doi.org/10.1021/la050499g.
[18] J.-R. Ku, S.-M. Lai, N. Ileri, P. Ramírez, S. Mafé, P. Stroeve, pH and ionic strength effects on amino acid transport through Au-nanotubule membranes charged with self-assembled monolayers, J. Phys. Chem. C 111 (2007) 2965–2973. https://doi.org/10.1021/jp066944d.
[19] J.A. Armstrong, E.E.L. Bernal, A. Yaroshchuk, M.L. Bruening, Separation of ions using polyelectrolyte-modified nanoporous track-etched membranes, Langmuir 29 (2013) 10287–10296. https://doi.org/10.1021/la401934v.
[20] A. Spende, N. Sobel, M. Lukas, R. Zierold, J.C. Riedl, L. Gura, I. Schubert, J.M. M. Moreno, K. Nielsch, B. Stühn, C. Hess, C. Trautmann, M.E. Toimil-Molares, TiO2 , SiO2 , and Al2O3 coated nanopores and nanotubes produced by ALD in etched ion-track membranes for transport measurements, Nanotechnology 26 (2015) 335301, https://doi.org/10.1088/0957-4484/26/33/335301.
[21] Yu Yamauchi, I.V. Blonskaya, P.Yu Apel, Osmosis in negatively charged nanocapillaries and its enhancement by an anionic surfactant, Colloid J. 80 (2018) 792–802, https://doi.org/10.1134/S1061933X19010162.
[22] A.V. Mitrofanov, A.V. Popov, D.V. Prokopovich, Track membranes and their replicas as high-frequency phase-contrast objects in X-ray optics, Radioelectron. Nanosyst. Inf. Technol. 12 (2020) 173–190, https://doi.org/10.17725/rensit.2020.12.173.
[23] A. Davis, J.H. Golden, Stability of polycarbonate, J. Macromol. Sci. Part C. 3 (1969) 49–68. https://doiorg/10/fswvsq.
[24] R.J. Morgan, J.E. O'Neal, The relationship between the physical structure and the mechanical properties of polycarbonate, J. Polym. Sci. Polym. Phys. Ed. 14 (1976) 1053–1076. https://doiorg/10/dm5h24.
[25] G.A. Adam, A. Cross, R.N. Haward, The effect of thermal pretreatment on the mechanical properties of polycarbonate, J. Mater. Sci. 10 (1975) 1582–1590. https://doiorg/10/fcjj8s.
[26] A. Hernandez, F. Martinez-villa, J.A. Ibañez, J.I. Arribas, A.F. Tejerina, An experimentally fitted and simple model for the pores in Nuclepore membranes, Separ. Sci. Technol. 21 (1986) 665–677. https://doi.org/10.1080/01496398608056142.
[27] C. Schonenberger, B.M.I. van der Zande, L.G.J. Fokkink, M. Henny, C. Schmid, M. Kruger, A. Bachtold, R. Huber, H. Birk, U. Staufer, Template synthesis of nanowires in porous polycarbonate membranes: electrochemistry and morphology, J. Phys. Chem. B 101 (1997) 5497–5505. https://doi.org/10.1021/jp963938g.

[28] E. Ferain, R. Legras, Characterisation of nanoporous particle track etched membrane, Nucl. Instrum. Methods Phys. Res. Sect. B Beam Interact. Mater. Atoms 131 (1997) 97–102. https://doi.org/10.1016/S0168-583X(97)00194-8.

[29] J. Duchet, R. Legras, S. Demoustier-Champagne, Chemical synthesis of polypyrrole: structure–properties relationship, Synth. Met. 98 (1998) 113–122. https://doi.org/10.1016/S0379-6779(98)00180-5.

[30] E. Ferain, R. Legras, Pore shape control in nanoporous particle track etched membrane, Nucl. Instrum. Methods Phys. Res. Sect. B Beam Interact. Mater. Atoms 174 (2001) 116–122. https://doi.org/10.1016/S0168-583X(00)00455-9.

[31] P. Apel, I. Blonskaya, S. Dmitriev, O. Orelovitch, B. Sartowska, Structure of polycarbonate track-etch membranes: origin of the "paradoxical" pore shape, J. Membr. Sci. 282 (2006) 393–400. https://doi.org/10.1016/j.memsci.2006.05.045.

[32] T.W. Cornelius, B. Schiedt, D. Severin, G. Pépy, M. Toulemonde, P.Y. Apel, P. Boesecke, C. Trautmann, Nanopores in track-etched polymer membranes characterized by small-angle x-ray scattering, Nanotechnology 21 (2010). https://doi.org/10.1088/0957-4484/21/15/155702.

[33] O. Glatter, O. Kratky, Small Angle X-Ray Scattering, Academic Press Inc., 1982.

[34] D.S. Sivia, Elementary Scattering theory : for X-Ray and Neutron Users, Cambridge University Press, 2011.

[35] A. Guinier, G. Fournet, Small-angle Scattering of X-Rays, 1989, https://doi.org/10.1016/0146-3535(89)90023-3.

[36] L.A. Feigin, D.I. Svergun, Structure Analysis by Small-Angle X-Ray and Neutron Scattering, Springer US, Boston, MA, 1987, https://doi.org/10.1007/978-1-4757-6624-0.

[37] P. Kluth, C.S. Schnohr, O.H. Pakarinen, F. Djurabekova, D.J. Sprouster, R. Giulian, M.C. Ridgway, A.P. Byrne, C. Trautmann, D.J. Cookson, K. Nordlund, M. Toulemonde, Fine structure in swift heavy ion tracks in amorphous SiO2, Phys. Rev. Lett. 101 (2008) 175503. https://doi.org/10.1103/PhysRevLett.101.175503.

[38] A. Hadley, C. Notthoff, P. Mota-Santiago, S. Dutt, S. Mudie, M.A. Carrillo-Solano, M.E. Toimil-Molares, C. Trautmann, P. Kluth, Analysis of nanometer-sized aligned conical pores using small-angle x-ray scattering, Phys. Rev. Mater. 4 (2020) 56003. https://doi.org/10.1103/PhysRevMaterials.4.056003.

[39] D. Schauries, M.D. Rodriguez, B. Afra, T. Bierschenk, C. Trautmann, S. Mudie, P. Kluth, Size characterization of ion tracks in PET and PTFE using SAXS, Nucl. Instrum. Methods Phys. Res. Sect. B Beam Interact. Mater. Atoms 365 (2015) 573–577. https://doi.org/10.1016/j.nimb.2015.08.071.

[40] G. Pépy, P. Boesecke, A. Kuklin, E. Manceau, B. Schiedt, Z. Siwy, M. Toulemonde, C. Trautmann, Cylindrical nanochannels in ion-track polycarbonate membranes studied by small-angle X-ray scattering, J. Appl. Crystallogr. 40 (2007) s388–s392. https://doi.org/10.1107/S0021889807000088.

[41] M. Engel, B. Stühn, J.J. Schneider, T. Cornelius, M. Naumann, Small-angle X-ray scattering (SAXS) off parallel, cylindrical, well-defined nanopores: from random pore distribution to highly ordered samples, Appl. Phys. Mater. Sci. Process 97 (2009) 99–108, 10/fh3vqm.

[42] U.H. Hossain, M.D. Rodriguez, D. Schauries, A. Hadley, M. Schleberger, C. Trautmann, S. Mudie, P. Kluth, SAXS investigation of un-etched and etched ion tracks in polycarbonate, Nucl. Instrum. Methods Phys. Res. Sect. B Beam Interact. Mater. Atoms 409 (2017) 293–297. https://doi.org/10.1016/j.nimb.2017.04.023.

[43] C. Dolfus, N. Piton, E. Toure, J.-C. Sabourin, Circulating tumor cell isolation: the assets of filtration methods with polycarbonate track-etched filters, Chin. J. Canc. Res. 27 (2015) 9.

[44] P.H.H. Lopez, R.L. Schnaar, Determination of glycolipid–protein interaction specificity. Methods Enzymol, Elsevier, 2006, pp. 205–220, https://doi.org/10.1016/S0076-6879(06)17015-9.

[45] M.-Y. Cheng, H.-H. Ho, T.-K. Huang, C.-F. Chuang, H.-Y. Chen, H.-W. Chung, W.-C. Leong, W.-C. Yang, C.-C. Fu, Y.-H. Hsu, Y.-C. Chang, A compartmentalized culture device for studying the axons of CNS neurons, Anal. Biochem. 539 (2017) 11–21. https://doi.org/10.1016/j.ab.2017.09.013.

[46] A. Delavari, D. Breite, A. Schulze, R.E. Baltus, Latex particle rejections from virgin and mixed charged surface polycarbonate track etched membranes, J. Membr. Sci. 584 (2019) 110–119. https://doi.org/10.1016/j.memsci.2019.04.065.

[47] H. Lee, D. Segets, S. Süß, W. Peukert, S.-C. Chen, D.Y.H. Pui, Liquid filtration of nanoparticles through track-etched membrane filters under unfavorable and different ionic strength conditions: experiments and modeling, J. Membr. Sci. 524 (2017) 682–690. https://doi.org/10.1016/j.memsci.2016.11.023.

[48] E.M. Bueno, J.W. Ruberti, Optimizing collagen transport through track-etched nanopores, J. Membr. Sci. 321 (2008) 250–263. https://doi.org/10.1016/j.memsci.2008.04.066.

[49] D.M. Kanani, W.H. Fissell, S. Roy, A. Dubnisheva, A. Fleischman, A.L. Zydney, Permeability–selectivity analysis for ultrafiltration: effect of pore geometry, J. Membr. Sci. 349 (2010) 405–410. https://doi.org/10.1016/j.memsci.2009.12.003.

[50] D. Kaya, K. Keçeci, Review—track-etched nanoporous polymer membranes as sensors: a review, J. Electrochem. Soc. 167 (2020), 037543. https://doi.org/10.1149/1945-7111/ab67a7.

[51] K. Kececi, N. San, D. Kaya, Nanopore detection of double stranded DNA using a track-etched polycarbonate membrane, Talanta 144 (2015) 268–274. https://doi.org/10.1016/j.talanta.2015.06.005.

[52] S. Jain, Highly sensitive detection of Salmonella typhi using surface aminated polycarbonate membrane enhanced-ELISA, Biosens. Bioelectron. 7 (2012). https://doi.org/10.1016/j.bios.2011.09.031.

[53] C.R. Martin, Z.S. Siwy, Learning nature's way: biosensing with synthetic nanopores, Science 317 (2007) 331–332. https://doi.org/10.1126/science.1146126.

[54] S. Faucher, N. Aluru, M.Z. Bazant, D. Blankschtein, A.H. Brozena, J. Cumings, J. Pedro de Souza, M. Elimelech, R. Epsztein, J.T. Fourkas, A.G. Rajan, H.J. Kulik, A. Levy, A. Majumdar, C. Martin, M. McEldrew, R.P. Misra, A. Noy, T.A. Pham, M. Reed, E. Schwegler, Z. Siwy, Y. Wang, M. Strano, Critical knowledge gaps in mass transport through single-digit nanopores: a review and perspective, J. Phys. Chem. C 123 (2019) 21309–21326. https://doi.org/10.1021/acs.jpcc.9b02178.

[55] K. Kim, Chemical and electrical characterization of virgin and protein-fouled polycarbonate track-etched membranes by FTIR and streaming-potential measurements, J. Membr. Sci. 134 (1997) 199–208, https://doi.org/10.1016/S0376-7388(97)00113-0.

[56] G. Pérez-Mitta, M.E. Toimil-Molares, C. Trautmann, W.A. Marmisollé, O. Azzaroni, Molecular design of solid-state nanopores: fundamental concepts and applications (accepted), Adv Mater (2019) 1–46, https://doi.org/10.1002/adma.201901483.

[57] D. Lee, A.J. Nolte, A.L. Kunz, M.F. Rubner, R.E. Cohen, pH-induced hysteretic gating of track-etched polycarbonate membranes: swelling/deswelling behavior of polyelectrolyte multilayers in confined geometry, J. Am. Chem. Soc. 128 (2006) 8521–8529. https://doi.org/10.1021/ja0608803.

[58] Y. Shen, P.O. Saboe, I.T. Sines, M. Erbakan, M. Kumar, Biomimetic membranes: a review, J. Membr. Sci. 454 (2014) 359–381. https://doi.org/10.1016/j.memsci.2013.12.019.

[59] S. Chaudhury, C. Agarwal, A.K. Pandey, A. Goswami, P.U. Sastry, Electrically-driven facilitated transport of Cs+ across copper ferrocyanide channels in track etched membrane, J. Membr. Sci. 434 (2013) 93–98. https://doi.org/10.1016/j.memsci.2013.01.038.

[60] P.S. Zhong, Aquaporin-embedded biomimetic membranes for nanofiltration, J. Membr. Sci. 7 (2012). https://doi.org/10.1016/j.memsci.2012.03.033.

[61] J. Won, S.K. Chae, J.H. Kim, H.H. Park, Y.S. Kang, H.S. Kim, Self-assembled DNA composite membranes, J. Membr. Sci. 249 (2005) 113–117. https://doi.org/10.1016/j.memsci.2004.08.031.

[62] W.A. Phillip, J. Rzayev, M.A. Hillmyer, E.L. Cussler, Gas and water liquid transport through nanoporous block copolymer membranes, J. Membr. Sci. 286 (2006) 144–152. https://doi.org/10.1016/j.memsci.2006.09.028.

[63] I. Huisman, P. Prádanos, J.I. Calvo, A. Hernández, Electroviscous effects, streaming potential, and zeta potential in polycarbonate track-etched membranes, J. Membr. Sci. 178 (2000) 79–92. https://doi.org/10.1016/S0376-7388(00)00485-3.

[64] C.-C. Ho, A.L. Zydney, Effect of membrane morphology on the initial rate of protein fouling during microfiltration, J. Membr. Sci. (1999) 15. https://doi.org/10.1016/S0376-7388(98)00324-X.

[65] P. Novo, M. Dell'Aica, M. Jender, S. Höving, R.P. Zahedi, D. Janasek, Integration of polycarbonate membranes in microfluidic free-flow electrophoresis, The Analyst 142 (2017) 4228–4239. https://doi.org/10.1039/C7AN01514C.

[66] P. Martínez-Pérez, J. García-Rupérez, Commercial polycarbonate track-etched membranes as substrates for low-cost optical sensors, Beilstein J. Nanotechnol. 10 (2019) 677–683. https://doi.org/10.3762/bjnano.10.67.

[67] C.R. Martin, Nanomaterials: a membrane-based synthetic approach, Science 266 (1994) 1961–1966. https://doi.org/10.1126/science.266.5193.1961.

[68] S. Valizadeh, J.M. George, P. Leisner, L. Hultman, Electrochemical synthesis of AgyCo multilayered nanowires in porous polycarbonate membranes. Thin Solid Films, 2002, p. 10. https://doi.org/10.1016/S0040-6090(01)01674-1.

[69] F. Maurer, A. Dangwal, D. Lysenkov, G. Müller, M.E. Toimil-Molares, C. Trautmann, J. Brötz, H. Fuess, Field emission of copper nanowires grown in polymer ion-track membranes, Nucl. Instrum. Methods Phys. Res. Sect. B Beam Interact. Mater. Atoms 245 (2006) 337–341. https://doi.org/10.1016/j.nimb.2005.11.124.

[70] B. Bercu, I. Enculescu, R. Spohr, Copper Tubes Prepared by Electroless Deposition in Ion Track Templates, 2004, p. 6. https://doi.org/10.1016/j.nimb.2004.06.011.

[71] M.E. Toimil-Molares, Characterization and properties of micro- and nanowires of controlled size, composition, and geometry fabricated by electrodeposition and ion-track technology, Beilstein J. Nanotechnol. 3 (2012) 860–883. https://doi.org/10.3762/bjnano.3.97.

[72] N. Naderi, M.R. Hashim, J. Rouhi, Synthesis and characterization of Pt nanowires electrodeposited into the cylindrical pores of polycarbonate membranes, Int J Electrochem Sci 7 (2012) 7.

[73] Z. Liu, S.Z.E. Abedin, M.S. Ghazvini, F. Endres, Electrochemical synthesis of vertically aligned zinc nanowires using track-etched polycarbonate membranes as templates, Phys. Chem. Chem. Phys. 15 (2013) 11362. https://doi.org/10.1039/C3CP51325D.

[74] X.-Q. Wei, G.F. Payne, X.-W. Shi, Y. Du, Electrodeposition of a biopolymeric hydrogel in track-etched micropores, Soft Matter 9 (2013) 2131. https://doi.org/10.1039/C2SM26898A.

[75] F. Nasirpouri, P. Southern, M. Ghorbani, A. Iraji zad, W. Schwarzacher, GMR in multilayered nanowires electrodeposited in track-etched polyester and polycarbonate membranes, J. Magn. Magn Mater. 308 (2007) 35–39. https://doi.org/10.1016/j.jmmm.2006.04.035.

[76] P. Ramirez, P.Y. Apel, J. Cervera, S. Mafe, Pore Structure and Function of Synthetic Nanopores with Fixed Charges: Tip Shape and Rectification Properties, 2008, p. 13. https://doi.org/10.1088/0957-4484/19/31/315707.

[77] N. Laohakunakorn, U.F. Keyser, Electroosmotic flow rectification in conical nanopores, Nanotechnology 26 (2015) 275202. https://doi.org/10.1088/0957-4484/26/27/275202.

[78] J.F. Pietschmann, M.T. Wolfram, M. Burger, C. Trautmann, G. Nguyen, M. Pevarnik, V. Bayer, Z. Siwy, Rectification properties of conically shaped nanopores: consequences of miniaturization, Phys. Chem. Chem. Phys. 15 (2013) 16917–16926. https://doi.org/10.1039/C3CP53105H.

[79] B. Balannec, A. Ghoufi, A. Szymczyk, Nanofiltration performance of conical and hourglass nanopores, J. Membr. Sci. 552 (2018) 336–340. https://doi.org/10.1016/j.memsci.2018.02.026.
[80] K.-L. Tung, Y.-L. Chang, C.-J. Chuang, Effect of pore morphology on fluid flow through track-etched polycarbonate membrane, Tamkang J. Sci. Eng. 4 (2001) 127–132.
[81] J.F. Ziegler, J.P. Biersack, The stopping and range of ions in matter, in: D. A. Bromley (Ed.), Treatise Heavy-Ion Sci., Springer US, Boston, MA, 1985, pp. 93–129, https://doi.org/10.1007/978-1-4615-8103-1_3.
[82] P. Mota-Santiago, H. Vazquez, T. Bierschenk, F. Kremer, A. Nadzri, D. Schauries, F. Djurabekova, K. Nordlund, C. Trautmann, S. Mudie, M.C. Ridgway, P. Kluth, Nanoscale density variations induced by high energy heavy ions in amorphous silicon nitride and silicon dioxide, Nanotechnology 29 (2018). https://doi.org/10.1088/1361-6528/aaabdb.
[83] M. Newville, R. Otten, A. Nelson, A. Ingargiola, T. Stensitzki, D. Allan, A. Fox, F. Carter, Michał, D. Pustakhod, S. Weigand Lneuhaus, R. Osborn, Glenn, C. Deil, Mark, A.L.R. Hansen, G. Pasquevich, L. Foks, N. Zobrist, O. Frost, A. Beelen, Kwertyops Stuermer, A. Polloreno, S. Caldwell, A. Almarza, A. Persaud, B. Gamari, B.F. Maier 2, Zenodo, 2021, https://doi.org/10.5281/ZENODO.4516651 lmfit/lmfit-py 1.0.
[84] B. Afra, M.D. Rodriguez, C. Trautmann, O.H. Pakarinen, F. Djurabekova, K. Nordlund, T. Bierschenk, R. Giulian, M.C. Ridgway, G. Rizza, N. Kirby, M. Toulemonde, P. Kluth, SAXS investigations of the morphology of swift heavy ion tracks in α-quartz, J. Phys. Condens. Matter 25 (2013) 45006. https://doi.org/10.1088/0953-8984/25/4/045006.
[85] C. Riedel, Spohr, R. Spohr, Statistical properties of etched nuclear tracks, Radiat. Eff. 42 (1979) 69–75. https://doi.org/10.1080/10420157908201738.
[86] J. Pfitzner, Poiseuille and his law, Anaesthesia 31 (1976) 273–275. https://doi.org/10.1111/j.1365-2044.1976.tb11804.x.
[87] G.M. Gusinskii, E.B. Kremer, M.I. Kremer, B.V. Mchedlishvili, Determination of the size of micropores in nuclear microfilters with small diameter, J. Eng. Phys. 37 (1979) 1493–1496. https://doi.org/10.1007/BF00859150.
[88] J.R. Welty, C.E. Wicks, R.E. Wilson, G.L. Rorrer, Fundamentals of Momentum, Heat and Mass Transfer, fifth ed., John Wiley and Sons, 2008. https://www.academia.edu/34116020/Welty_Fundamentals_Momentum_Heat_Mass_Transfer_5th_txtbk.PDF.
[89] N. Sertova, E. Balanzat, M. Toulemonde, C. Trautmann, Investigation of initial stage of chemical etching of ion tracks in polycarbonate, Nucl. Instrum. Methods Phys. Res. Sect. B Beam Interact. Mater. Atoms 267 (2009) 1039–1044. https://doi.org/10.1016/j.nimb.2009.02.045.
[90] P. Apel, A. Schulz, R. Spohr, C. Trautmann, V. Vutsadakis, Track size and track structure in polymer irradiated by heavy ions, Nucl. Instrum. Methods Phys. Res. Sect. B Beam Interact. Mater. Atoms 146 (1998) 468–474. https://doi.org/10.1016/S0168-583X(98)00445-5.
[91] P. Apel, Swift ion effects in polymers: industrial applications, Nucl. Instrum. Methods Phys. Res. Sect. B Beam Interact. Mater. Atoms 208 (2003) 11–20. https://doi.org/10.1016/S0168-583X(03)00634-7.
[92] P.Y. Apel, I.V. Blonskaya, V.R. Oganessian, O.L. Orelovitch, C. Trautmann, Morphology of latent and etched heavy ion tracks in radiation resistant polymers polyimide and poly(ethylene naphthalate), Nucl. Instrum. Methods Phys. Res. Sect. B Beam Interact. Mater. Atoms 185 (2001) 216–221. https://doi.org/10.1016/S0168-583X(01)00967-3.
[93] D. Fink, Transport Processes in Ion-Irradiated Polymers, Springer Berlin Heidelberg, Berlin, Heidelberg, 2004, https://doi.org/10.1007/978-3-662-10608-2.
[94] A. Hadley, Characterisation of Ion Track-Etched Solid-State Nanopores Using Small Angle X-Ray Scattering, Australian National University, 2020. https://openresearch-repository.anu.edu.au/handle/1885/216848.
[95] P. Kluth, O.H. Pakarinen, F. Djurabekova, R. Giulian, M.C. Ridgway, A.P. Byrne, K. Nordlund, Nanoscale density fluctuations in swift heavy ion irradiated amorphous SiO_2, J. Appl. Phys. 110 (2011) 123520, https://doi.org/10.1063/1.3671614.